

# Super-resolution microscopy on single particles at fluid interfaces reveals their wetting properties and interfacial deformations

## – Supplementary Information –

A. Aloï,<sup>\*a,b,c</sup> N. Vilanova,<sup>a,c</sup> L. Isa,<sup>d</sup> A.M. de Jong,<sup>a,e</sup> and I.K. Voets,<sup>\*a,b,c,f</sup>

<sup>a</sup> Institute for Complex Molecular Systems, Eindhoven University of Technology, Post Office Box 513, 5600 MB Eindhoven, The Netherlands.

<sup>b</sup> Laboratory of Self-Organizing Soft Matter, Department of Chemistry and Chemical Engineering, Eindhoven University of Technology, Post Office Box 513, 5600 MB Eindhoven, The Netherlands.

<sup>c</sup> Laboratory of Macromolecular and Organic Chemistry, Department of Chemistry and Chemical Engineering, Eindhoven University of Technology, Post Office Box 513, 5600 MB Eindhoven, The Netherlands.

<sup>d</sup> Laboratory for Interfaces, Soft Matter and Assembly, Department of Materials, ETH Zurich, Vladimir-Prelog Weg 5, 8093 Zürich, Switzerland.

<sup>e</sup> Laboratory of Molecular Biosensing, Department of Applied Physics, Eindhoven University of Technology, Post Office Box 513, 5600 MB Eindhoven, The Netherlands.

<sup>f</sup> Laboratory of Physical Chemistry, Department of Chemistry and Chemical Engineering, Eindhoven University of Technology, Post Office Box 513, 5600 MB Eindhoven, The Netherlands.

\*[A.Aloi@tue.nl](mailto:A.Aloi@tue.nl)

\*[I.Voets@tue.nl](mailto:I.Voets@tue.nl)

# Contents

<b>1. iPAINT method applied to visualize particles at fluid interfaces.</b>	
<b>1.1 iPAINT localization accuracy.....</b>	<b>4</b>
<b>2. Monitoring the sliding of the interface towards the steady-state.....</b>	<b>5</b>
<b>3. Spherical particles.....</b>	<b>7</b>
<b>3.1 Synthesis and SEM characterization of silica particles.....</b>	<b>7</b>
<b>3.1.1 AFM characterization of silica particles.....</b>	<b>8</b>
<b>3.2 Calculation of contact angle of individual spherical particles.....</b>	<b>9</b>
<b>3.3 Narrow single particle contact angle distribution.....</b>	<b>11</b>
<b>3.4 Extended contact angles and line tension data of hydrophobic and hydrophilic particles.....</b>	<b>15</b>
<b>3.5 Impact of the iPAINT probe on the single-particle contact angle measurement.....</b>	<b>16</b>
<b>3.5.1 Interfacial tension and macroscopic contact angle measurements.....</b>	<b>17</b>
<b>4. Ellipsoidal particles.....</b>	<b>19</b>
<b>4.1 Synthesis and TEM characterization of polystyrene ellipsoidal particles.....</b>	<b>19</b>
<b>4.2 Calculation of contact and polar angles of individual ellipsoidal particles.....</b>	<b>20</b>
<b>4.3 Quantifying the orientation of ellipsoids at the liquid-liquid interface.....</b>	<b>22</b>
<b>4.4 Single ellipsoidal particle contact angle measurement.....</b>	<b>23</b>
<b>4.5 Pivoting of ellipsoids at the fluid interface.....</b>	<b>24</b>
<b>5. References.....</b>	<b>25</b>

## 1. iPAINT method applied to visualize particles at fluid interfaces.

Fig. S1 shows a flow chart of a typical iPAINT experiment to visualize particles adsorbed at fluid interfaces. A large reservoir of polyethylene glycol chains end-functionalized with a photo-activatable probe (PEG-552) is present in solution. The majority of these macromolecules diffuses freely in the water solution. The iPAINT probes adsorb and desorb at all the relevant interfaces, non-covalently labelling the interfaces during imaging. Initially, no fluorescence signal is collected since the probes are in a dark, non-fluorescent, state (left panel in Fig. S1). Subsequently, a low-power UV laser triggers the photo-activation of a small subset of probes, both in solution and adsorbed at interfaces. At the same time, a full-power readout beam selectively excites the photo-activated probes (middle panel in Fig. S1). By changing the power of the UV laser, the number of fluorescent dyes in the bright state is tuned. The localization of single molecules occurs exclusively at the interfaces (red crosses in the middle panel in Fig. S1). This is because iPAINT probes in solution diffuse too fast to be captured with high accuracy by the EMCCD camera at the set acquisition rate. A continuous repetition of the aforementioned steps leads to the reconstruction of particles and fluid interfaces with nanometer accuracy.

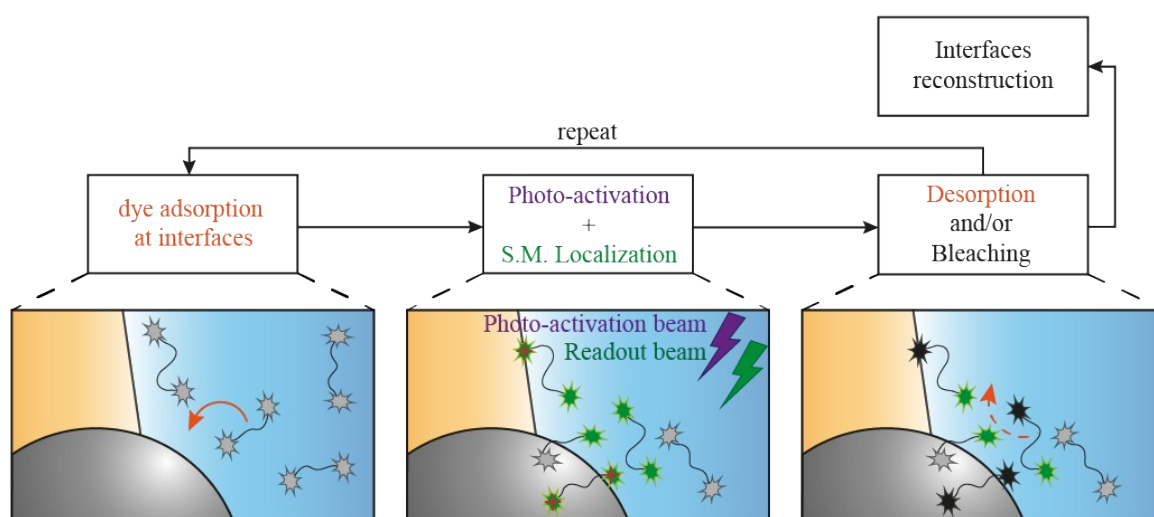


**Fig. S1** Flow chart of an iPAINT experiment starting with the adsorption of the iPAINT probes at solid and fluid interfaces followed by photo-activation, excitation, single molecule (S.M.) localization, desorption and/or bleaching of the dye, leading to the full reconstruction of the interfaces.

### 1.1 iPAINT localization accuracy.

The spatial resolution on single molecule localizations depends on the total number on several factors, as explained by eq. S1:<sup>[1]</sup>

$$\sigma_{\mu_i} = \sqrt{\frac{s_i^2}{N} + \frac{a^2/12}{N} + \frac{8\pi s_i^4 b^2}{a^2 N^2}} \propto \frac{s_i}{\sqrt{N}} \quad (S1)$$

Here,  $\sigma$  is the standard error calculated on the mean of the photon distribution ( $\mu = x_0; y_0$ ),  $a$  is the effective pixel size of the EMCCD camera,  $b$  is the RMS background noise,  $s_i$  is the standard deviation of the localization distribution (in direction  $i$ , with  $i = x$  or  $y$ ), and  $N$  is the number of photons

collected. Typically the noise term due to pixelation  $\left(\frac{a^2/12}{N}\right)$  and the background noise  $\left(\frac{8\pi s_i^4 b^2}{a^2 N^2}\right)$  are negligible when compared to shot noise. Thus, equation S1 can be simplified by omitting the second and the third term and be approximated to the inverse of the number of photons emitted by each single molecule. Fig. S2 shows the histogram of the photon counts for two exemplary iPAINT images of hydrophobic (Fig. S2a) and hydrophilic (Fig. S2b), respectively. Independently to the type of particles imaged the resolution on the technique is the same.

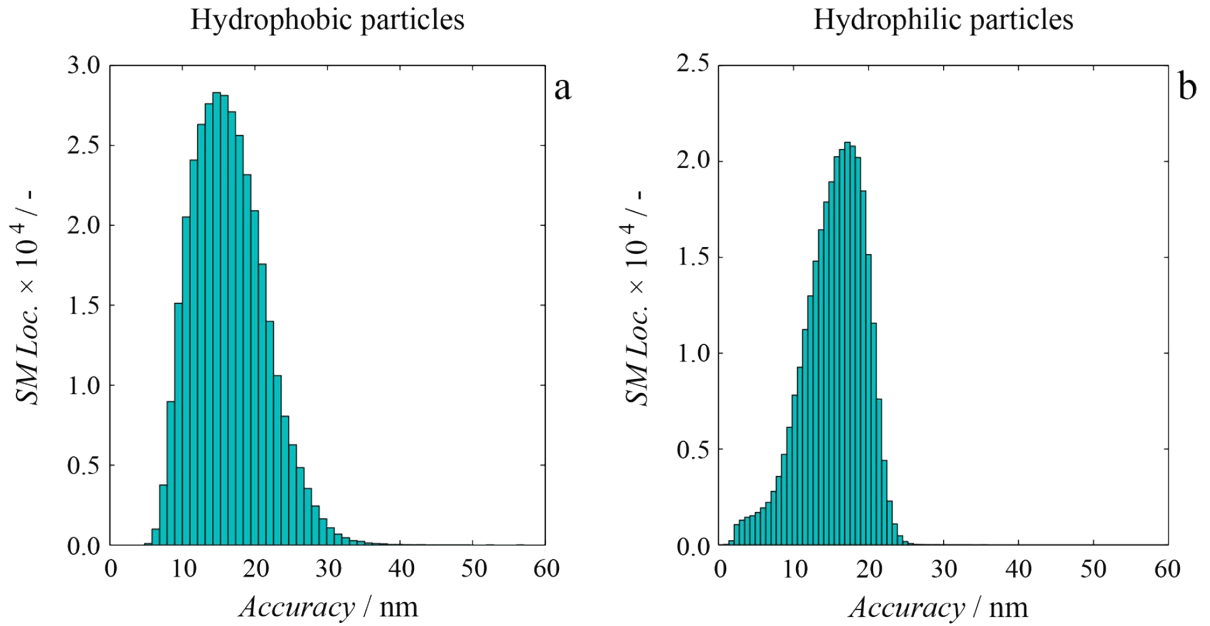


**Fig. S2** Theoretical single molecule localization accuracy calculated for (a) hydrophobic and (b) hydrophilic silica particles when adsorbed at water-octanol interface. Mean value of the distributions: 15nm and 17nm, respectively.

## 2. Monitoring the sliding of the interface towards the steady-state.

Accurate particle and interface localization necessitates imaging under stable conditions. To this end, we first determine the position of the interface by wide-field imaging, after which we monitor the sliding of the interface during the transition towards the steady-state. This serves as a test of potential pinning of the interface on the coverslip due to particle adsorption and enables us to determine the time it takes to reach steady-state conditions. We prepare a sample by bringing into contact a droplet of the aqueous solution of particles and PEG-552 and an oil droplet. The location of the interface is determined from an intensity profile of a wide-field image of the two liquids in contact (Fig. S3).

The aqueous phase, oil phase, and interface, can be distinguished in the fluorescence intensity profile based on their grayscale values (Fig. S3b), which is maximal at the interface ( $\sim 60$ ) and lower in the respective bulk phases, water ( $\sim 40$ ) and oil ( $\sim 20$ ). This method enables interface localization with a  $\sim 1 \mu\text{m}$  accuracy (Fig. S3b). Next, we collect the time-lapse images of the particles and interface in wide-field (Fig. S3c-h), and monitor the sliding of the interface (greyscale value  $\sim 60$ ) and adsorbed particles (greyscale value  $\sim 150-200$ ) during 45 minutes. We observe the motion of the interface (white dashed line in Fig. S3c-h) and the particles thereby adsorbed moving in the same direction in time. To trace the correlated motion of the interface and the particles thereby adsorbed, we measure the fluorescence intensity profiles along the double-arrowed lines shown in Fig. S3c-h, and plot them as function of their position (Fig. S3j). The unidirectional motion of interface and particles demonstrates that the interface is not pinned. Instead, both the particles and the interface can adjust their position and transition towards a steady-state condition. We monitor the sliding of the interface and the particles during 45 minutes to determine how long it takes to reach steady-state. we find the interface at similar positions at  $t = 5.42 \text{ s}$  and  $t = 45 \text{ min}$ , suggesting that steady-state is reached within a few seconds after sample preparation. To be certain iPAINt imaging is performed under steady-state conditions, we nevertheless initiate image acquisition 1 hour after sample preparation.

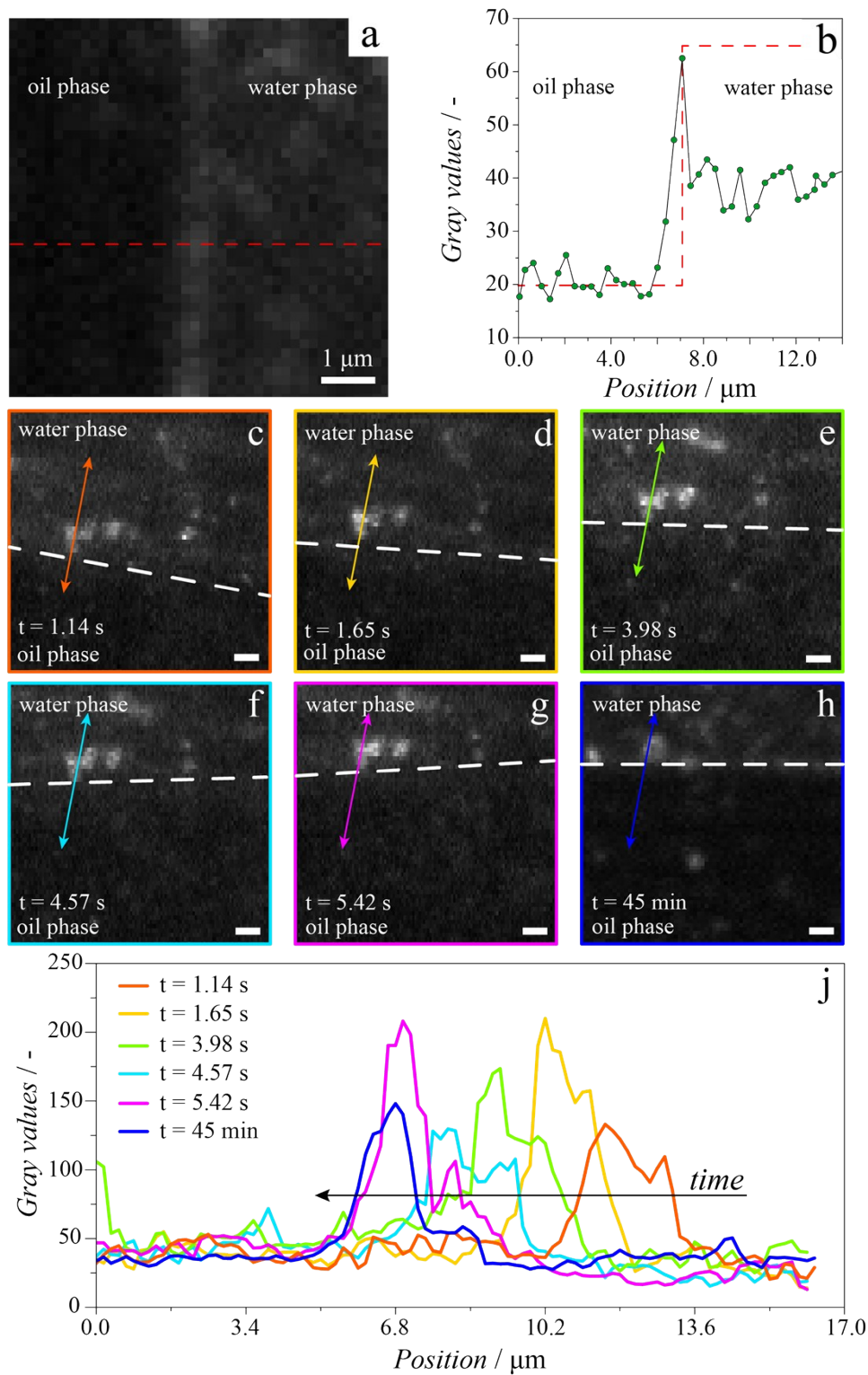


**Fig. S3:** Identification of the fluid interface and its sliding. (a) Wide-field image of the oil-water interface. The water phase is rich in PEG-552 probes and hence fluorescent; the oil phase appears darker. (b) Intensity profile along the dashed red line in (a); from the grey values the position of the interface can be defined. (c-h) Wide-field images of hydrophilic colloidal particles adsorbed at the water-octanol interface visualized over 45 min. The dashed white line indicates the position of the fluid interface, between the aqueous and the octanol phases. The double-angled line indicates the direction along which the fluorescence intensity traces presented in (j) have been recorded. (j) Fluorescence intensity signal along the double-angled line as a function of pixel position.

### 3. Spherical particles

#### 3.1 Synthesis and SEM characterization of silica colloids

Hydrophilic silica beads of  $\sim 330$  nm in radius are synthesized using a two-step Stöber-based method.<sup>[2]</sup> Silica particles with intermediate hydrophobicity are obtained by partially functionalizing them with stearyl alcohol through a modified van Helden method.<sup>[3]</sup>

Briefly, 0.25 g of hydrophilic particles are dispersed by sonication in ethanol together with 0.07 mg of stearyl alcohol and 0.70 g octadecane. Subsequent evaporation of ethanol is achieved under a stream of air. The system is then heated up to 180 °C for 6 hours under an inert atmosphere. Because of the high temperature, the octadecane melts and acts as solvent allowing the stearyl alcohol chains to react with the silanol groups onto the silica colloids. The applied 1:10 ratio stearyl alcohol:octadecane ensures an incomplete hydrophobization of the particles. The resulting particles are thoroughly washed with chloroform and dried overnight at 70 °C in vacuum. All chemicals are purchased from Sigma-Aldrich and used without further purification.

A FEI Quanta 600F ESEM scanning electron microscope (SEM) is used to image the silica particles. Fig. S4 shows a SEM image of the colloids, where the inset illustrates the size distribution obtained from image analysis of more than 100 particles. The image analysis is run using Image-J; a mean radius  $\bar{R} = 332 \pm 14$  nm is computed.

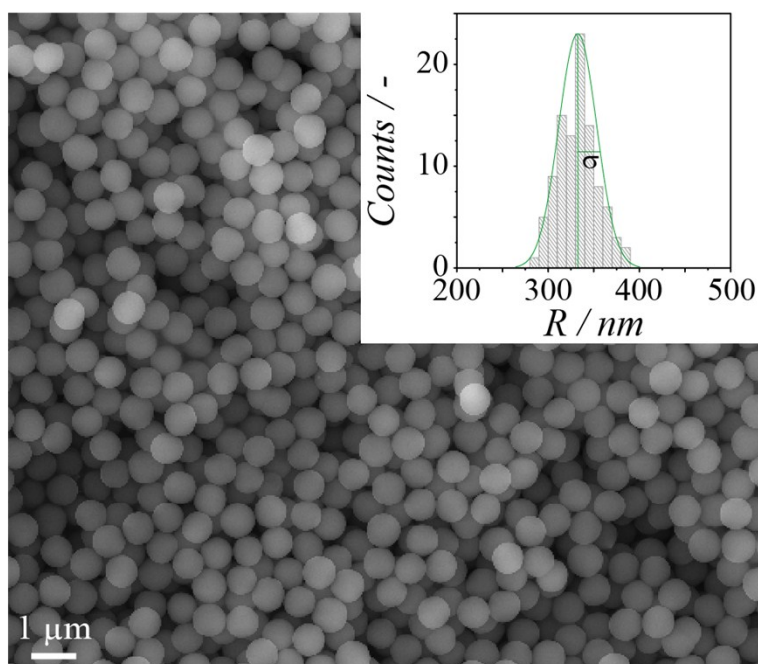


**Fig. S4** Characterization of silica colloids. SEM pictures of plain silica beads of  $\sim 330$  nm in radius. The inset shows the distribution of the particle radius measured for over 100 beads.

We additionally measured the  $\zeta$ -potential of both type of particles in their pristine state and in presence of iPAINT probes. To compare the surface charges of hydrophilic and hydrophobic particles, all  $\zeta$ -potential measurements (Smoluchowski model) were performed in aqueous solutions.

Partial functionalization with stearyl alcohol chains allows hydrophobic particles to still be dispersed in an aqueous solution. We report in the following table the obtained results (mV):

	Hydrophilic	Hydrophilic + PEG552	Hydrophobic	Hydrophobic + PEG552
In KCl (1 mM)	$-68.4 \pm 1.1$	$-49.2 \pm 0.3$	$-48.5 \pm 1.8$	$-32.5 \pm 0.7$

The addition of the iPAINT probe results in a decrease of the negative charges on the surface of both type of particles. This is most likely due to the combination of the following two factors: i) positive charge carried by the photoactivatable moiety (Cage-552) and ii) possible screening of the overall charges by PEG chains.

### 3.1.1 AFM characterization of silica particles.

The surface roughness of the particles used in our iPAINT experiment was characterized by AFM in dry conditions. Particles were dispersed in milli-Q water with a  $0.5 \mu\text{M}$  solution of iPAINT probes, to mimic the status of the particles at the fluid interface during iPAINT imaging. We measured an average roughness (calculated over 10 lines across the surface of the particles) of 3.3 nm and 2.6 nm for the hydrophilic and hydrophobic particles, respectively. The RMS (root mean squared) roughness is 0.77 nm for the hydrophilic particles, and 0.49 nm for the hydrophobic one (Fig. S5).

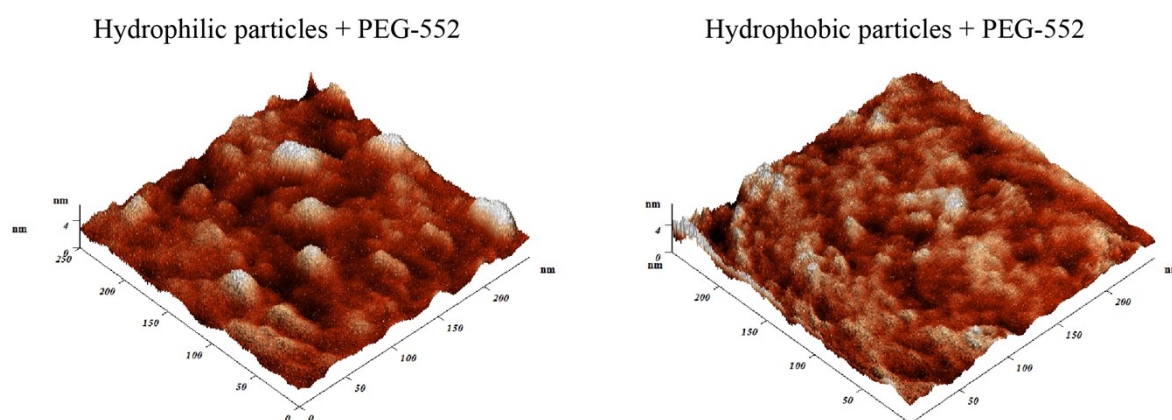


**Fig. S5** AFM imaging of the surface of hydrophilic and hydrophobic particles in presence of PEG-552 probes adsorbed on their surface.

### 3.2 Calculation of contact angle of individual spherical particles

We use two different strategies to compute the contact angle,  $\theta$ , for the hydrophilic and hydrophobic particles. In the case of hydrophilic particles, these are completely labelled since they are dispersed in the water phase along with the PEG-552. In this case, we isolate the particles based on the density of single-molecule localization (as described in the main text, Fig. 2), and proceed to fit the particle to a circle running a Matlab routine called 'Circle Fit'. Here, the algorithm minimizes the quantity:  $\sum (x^2 + y^2 - R^2)^2$ . The fit gives the  $(x, y)$  coordinates of the center of the particle, and its radius,  $R$ . To determine the position of the particle compared to the interface, we first select the single-molecule localizations which belong to the interface. By sectioning across the interface (red rectangles in Fig. S6a), the localizations appear to follow a Gaussian profile (Fig. S6b), and its mean value is taken as the most probable location of the interface. This procedure is applied all along the interface (every  $\sim 20$  nm interval) to determine its profile. By overlapping the profile of the interface with the position of the particles (Fig. S6c), we can calculate  $h$ , the height of the hydrophilic particles in the oil phase. The computed values of  $h$ , and the radii of the particles obtained from the 2D fit are subsequently used in the following equation to calculate the contact angle,  $\theta$ :

$$\theta_{hydrophilic} = \cos^{-1} \left( \frac{R - h}{R} \right). \quad (S2)$$

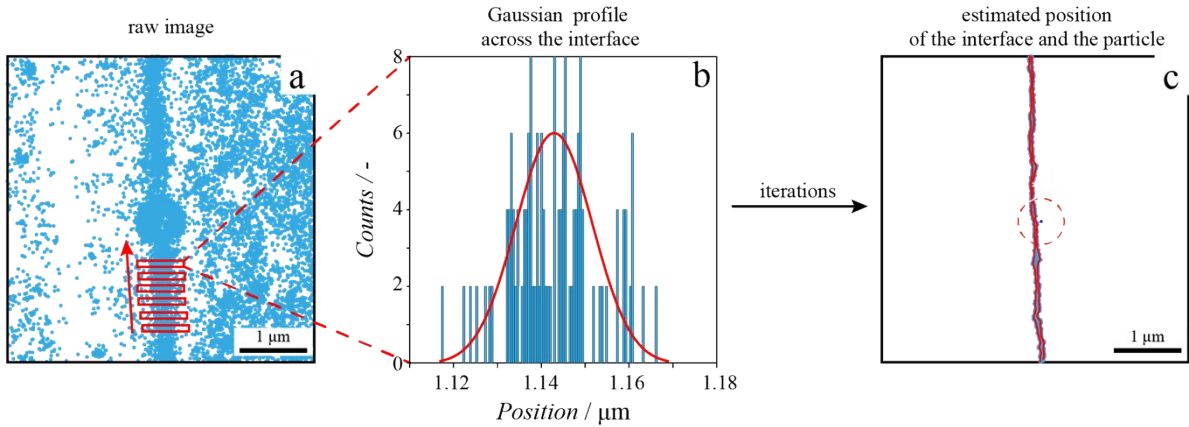


**Fig. S6** Analysis routine to compute the contact angle of hydrophilic particles at a fluid interface. (a) Representative iPAINT image of a hydrophilic particle adsorbed at a fluid interface. The red rectangles illustrate the sectioning across the interface, along the red arrow, to determine its location. (b) Distribution of localizations in one of the red rectangles presented in (a); the mean value gives the most probable location of the interface. (c) Reconstructed interface, and placement of the circle fitting the particle. From (c) the height,  $h$ , of the particle in the oil phase is calculated, giving in turn the contact angle,  $\theta$ .

Conversely, for hydrophobic particles, only the hemisphere exposed to the water phase is labelled by PEG-552 probes, and hence visible. Here, the principal dimensions which can be determined from iPAINT images are the height,  $h$ , and the lateral size,  $2l$  (Fig. S7). We can calculate from trigonometry the radius of the particle,  $R$ , according to eq. S3:

$$(R - h)^2 = R^2 - l^2. \quad (S3)$$

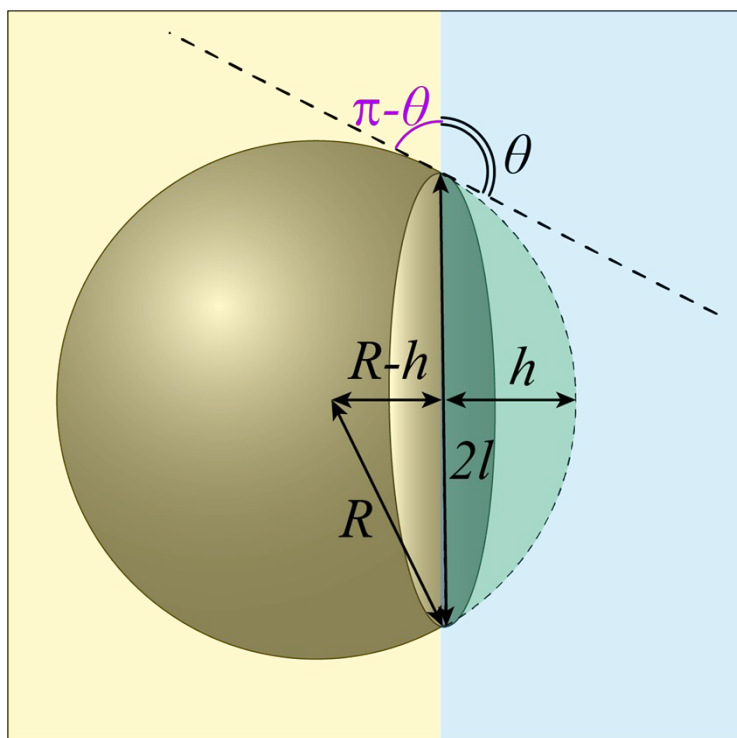


**Fig. S7** Representative cartoon of an hydrophobic spherical particle at a fluid interface. The dimensions needed to calculate the contact angle are illustrated by the double-headed segments in black and summarized in eq. S2.

The measured  $h$  and the calculated radii,  $R$ , are then used to compute the contact angle for each single hydrophobic particle:

$$\theta_{hydrophobic} = \cos^{-1} \left( \frac{h-R}{R} \right). \quad (S4)$$

In the case of hydrophobic particles the error on the size distribution of the radius of the particles is higher than the one computed for the hydrophilic particles due to the method used to calculate  $R$ . In fact, for the hydrophobic particles we have to consider the errors on the determination of  $h$  and  $2l$ . Whereas, for the hydrophilic particles the error is the standard deviation on the size of the particles obtained through the fitting routine run in Matlab.

### 3.3 Narrow single particle contact angle distribution

Multiple factors may cause the broadening of the contact angle distribution, some of which are related to the colloidal particles,  $\sigma_{\theta,p}$  (chemical heterogeneities, size polydispersity),<sup>[4]</sup> and others to the liquid-liquid interface (aging of the three-phase contact line and and/or thermal motion of the particle within the oil-water interfacial plane,  $\sigma_{\theta,B}$ ).<sup>[5-7]</sup> In addition, the limited experimental resolution of iPAINT,  $\sigma_{\theta,res,i}$ , should be taken into account. Taking a closer look at the contact angle distributions obtained by iPAINT (Fig. 3 in the main text) is therefore of interest.

We first critically evaluate whether aging effects can safely be neglected. We measure the average contact angle,  $\bar{\theta}$ , of the overall population of both particle types as a function of time (Fig. S8). The contact angle remains fairly constant during the course of several hours, aside from small fluctuations which are within the experimental uncertainty. Hence, no significant aging is observed for the overall population of colloids, and can be ruled out from the contact angle distributions ( $\sigma_{\theta,B} = 0$ ).

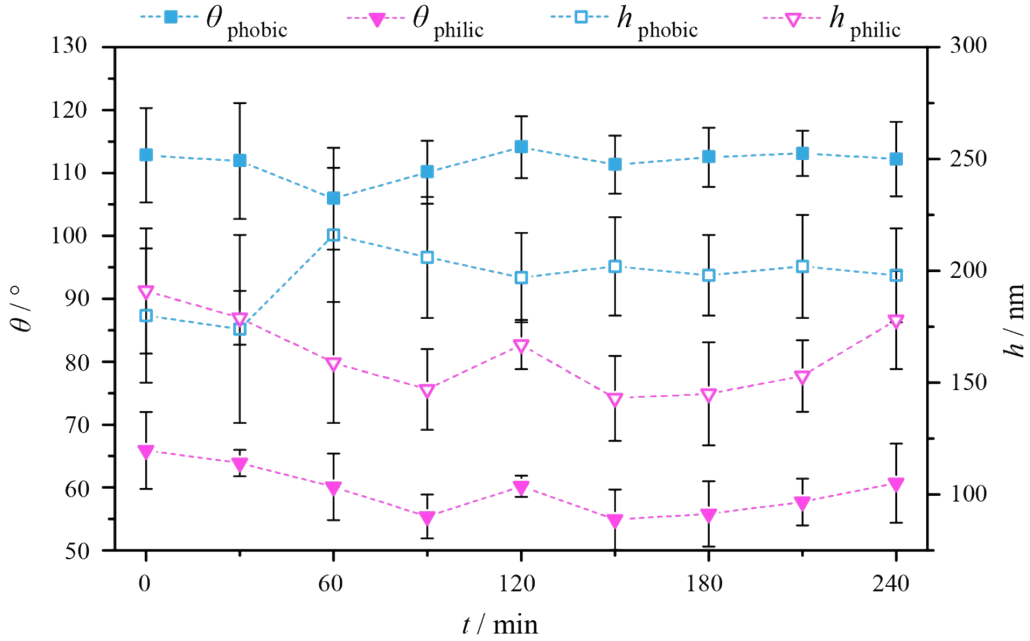


**Fig. S8** Variation in time of the total population of the contact angle,  $\bar{\theta}$ , (close symbols) and the height,  $h$ , (open symbols) of different particles in the same sample relative to the position of the interface for hydrophobic (cyan symbols) and hydrophilic (magenta symbols) particles. The graph suggests that no aging of the contact line occurs.

The parameter of interest is  $\sigma_{\theta,p}$ , as this variability in particle position is related to differences in particle size and surface functionalization. The factors affecting the total broadening of the contact angle distribution in iPAINT can be described by the following equation:

$$\sigma_{\theta,total,i} = \sqrt{\sigma_{\theta,res,i}^2 + \sigma_{\theta,p}^2 + \sigma_{\theta,B}^2} \quad (S5)$$

Since the particles' adsorption energy  $\Delta E \gg k_B T$ , and the particles are immobilized at the coverslip, Brownian motion can safely be neglected ( $\sigma_{\theta,B} \ll \sigma_{\theta,res,i}, \sigma_{\theta,p}$ ). Hence,  $\sigma_{\theta,p}$  can be calculated from eq. S4 and the measured  $\sigma_{\theta,total,i}$ , once  $\sigma_{\theta,res,i}$  is computed.

$\sigma_{\theta,res,i}$  is determined by the accuracy of the single-molecule localizations from which the radius,  $R$ , and the height of the spherical cap,  $h$ , are obtained, since these are the quantities needed to calculate the contact angle, according to eqs. S2 and S4. We refer to these two quantities as  $\sigma_{R,res,i}$  and  $\sigma_{h,res,i}$ . First, we determine  $\sigma_{R,res,i}$ . To do so, we measure the size distribution of particles calculated by SEM imaging (blue curves in Fig. S9a and S9c) and its standard deviation ( $\sigma_{R,p,e}$ ). Here we assume that the SEM distribution is given only by the polydispersity of the particles ( $\sigma_{R,p}$ ), *i.e.*, the resolution of the method does not broaden the width of the distribution ( $\sigma_{R,p,e} = \sigma_{R,p}$ ). Conversely, the particle size distribution ( $\sigma_{R,p,i}$ ) obtained by iPAINT imaging of the same particles (red curve in Fig. S9a and S9c) are broadened by the polydispersity of the particles ( $\sigma_{R,p}$ ) and by the accuracy of the single-molecule localizations ( $\sigma_{R,res,i}$ ).

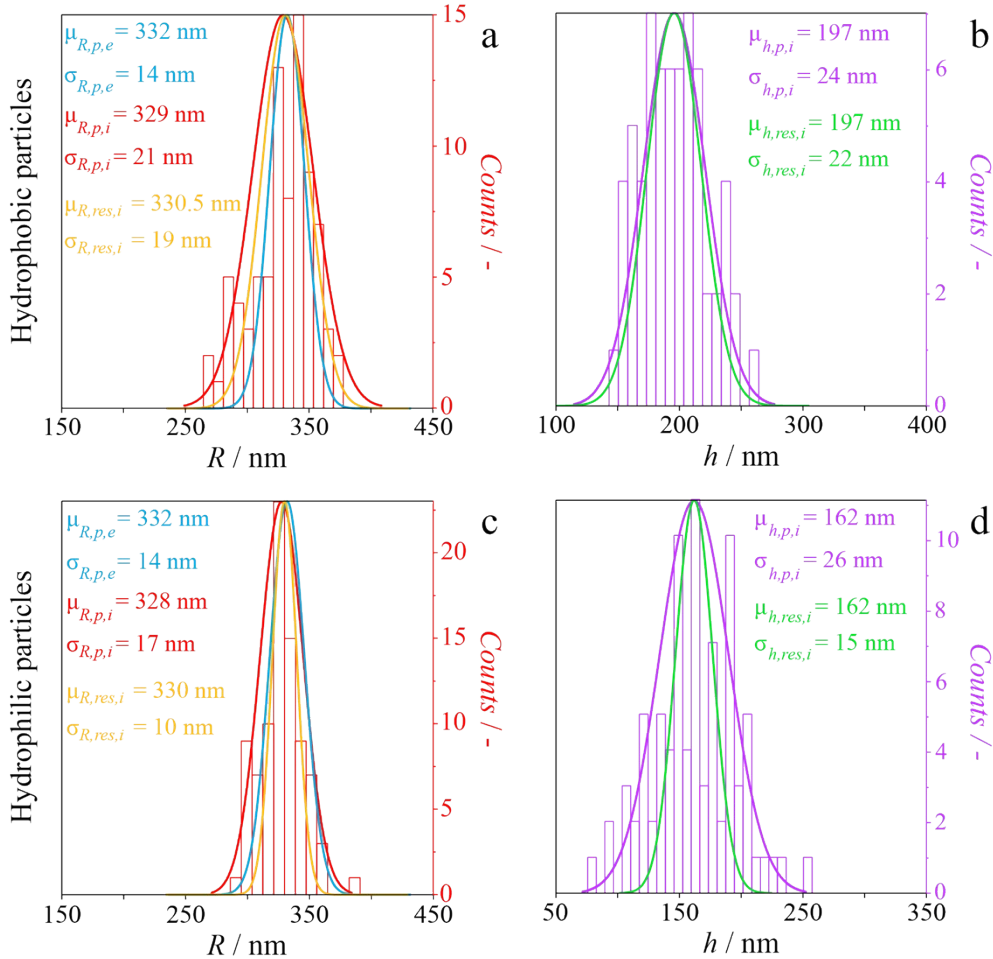


**Fig. S9** Influence of iPAINT resolution on estimating size distributions. (a, c) Size distribution of colloidal particles imaged by SEM (blue curve), and by iPAINT (red curve and histogram data). The yellow curve is given by deconvolution between the blue and the red curve, and illustrates the distribution in sizes of particles only affected by iPAINT resolution. (b, d) Size distribution of heights of the spherical cap of colloidal particles

adsorbed at the liquid-liquid interface, before (purple curve and histogram data) and after (green curve) deconvolution. The Gaussian curves are normalized to their maxima for visualization reasons.

Hence, we can calculate  $\sigma_{R,res,i}$  from the deconvolution of  $\sigma_{R,p,e}$  (blue distributions in Fig. S9) and  $\sigma_{R,p,i}$  (red distributions in Fig. S9):

$$\sigma_{R,res,i} = \sqrt{\sigma_{R,p,i}^2 - \sigma_{R,p,e}^2} \quad (S6)$$

This gives  $\sigma_{R,res,i} = 19$  nm for the hydrophobic particles,  $\sigma_{R,res,i} = 10$  nm for the hydrophilic particles. Now that  $\sigma_{R,res,i}$  is determined, we compute how the resolution in iPAINT affects the distribution of heights of the spherical caps (green curve in Fig. S9b and S9d), and its width ( $\sigma_{h,res,i}$ ). To do so, we rescale  $\sigma_{R,res,i}$  to the experimental data of  $h$  (purple curve in Fig. S9b and S9d). The results of the radii and the heights are summarized in Table S1:

**Table S1** Mean ( $\mu_R$ ) and standard deviations ( $\sigma_R$ ) of the size distributions of hydrophobic and hydrophilic colloidal particles obtained by SEM, iPAINT and from their deconvolution. Mean ( $\mu_h$ ) and standard deviations ( $\sigma_h$ ) of the distribution of the spherical cap height of hydrophobic and hydrophilic colloidal particles, obtained by iPAINT and their deconvolution with the iPAINT resolution.

Particle	Particle Radius			Spherical Cap Height		
	Distribution	$\mu_R$ (nm)	$\sigma_R$ (nm)	Distribution	$\mu_h$ (nm)	$\sigma_h$ (nm)
Hydrophobic	$R,p,e$	332	14	-	-	-
	$R,p,i$	329	21	$h,p,i$	197	24
	$R,res,i$	330.5	19	$R,res,i$	197	22
Hydrophilic	$R,p,e$	332	14	-	-	-
	$R,p,i$	328	17	$h,p,i$	162	26
	$R,res,i$	330	10	$R,res,i$	162	15

Now that both  $\sigma_{R,res,i}$  and  $\sigma_{h,res,i}$  are known, we can finally compute  $\sigma_{\theta,res,i}$  as:

$$\begin{aligned} \sigma_{\theta,res,i} &= \sqrt{\left(\left|\frac{\partial\theta}{\partial R}\right|\partial R\right)^2 + \left(\left|\frac{\partial\theta}{\partial h}\right|\partial h\right)^2} = \\ &= \sqrt{\left(\frac{|h-R|^2 + R(h-R)}{R^2|h-R|} \sqrt{1 - \frac{|h-R|^2}{R^2}} \partial R\right)^2 + \left(\frac{R-h}{R|h-R|} \sqrt{1 - \frac{|h-R|^2}{R^2}} \partial h\right)^2} \quad (S7) \end{aligned}$$

where  $\partial R$  and  $\partial h$  are the standard deviation on the radii ( $\sigma_{R,res,i}$ ) and heights ( $\sigma_{h,res,i}$ ) affected by the iPAINT resolution, as calculated from the distributions in Fig. S9. We obtain  $\sigma_{\theta,res,i} = 6.6^\circ$  for the hydrophobic particles and  $\sigma_{\theta,res,i} = 4.2^\circ$  for the hydrophilic ones.

Using these computed values and the standard deviations of the measured distributions of contact angles shown in Fig. 3 in the main text ( $\sigma_{\theta,total,i} = 7.0^\circ$  for the hydrophobic particles, and  $\sigma_{\theta,total,i} = 6.9^\circ$  for the hydrophilic ones), we can determine the effect of the particle variability ( $\sigma_{\theta,p}$ ) on the broadening of the contact angle distributions. To do so, we compute  $\sigma_{\theta,p}$  from eq. S4, which

gives  $\sigma_{\theta,p} = 2.3^\circ$  for the hydrophobic particles (red curve in Fig. S10a), and  $\sigma_{\theta,p} = 5.5^\circ$  for the hydrophilic ones (red curve in Fig. S10b).

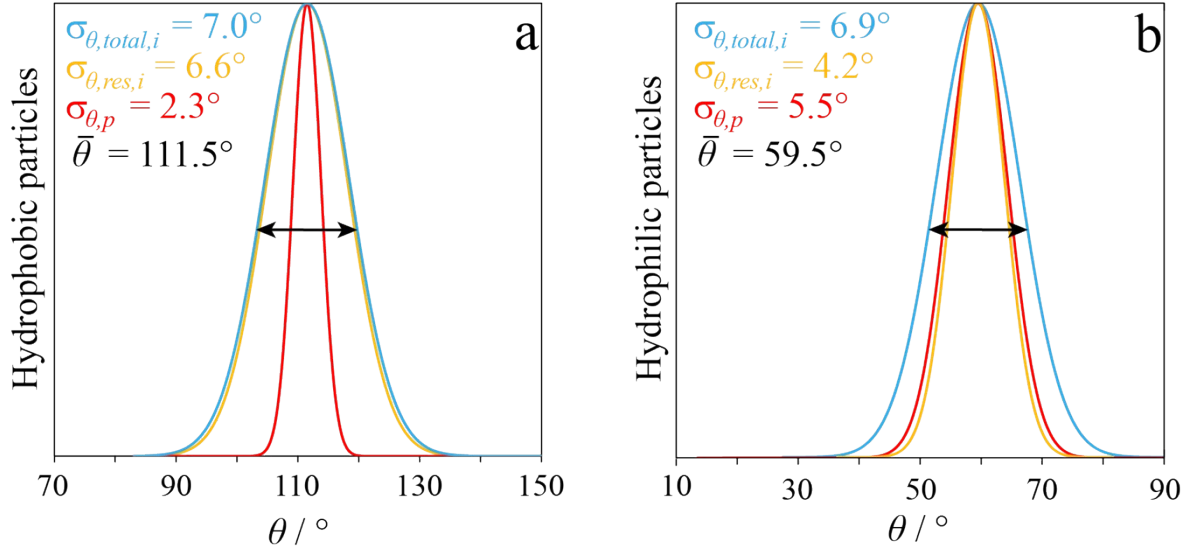


**Fig. S10** Influence of the iPAINT resolution ( $\sigma_{\theta,res,i}$ ), and the variability of the particle position relative to the interface ( $\sigma_{\theta,p}$ ) on determining the contact angle distributions for (a) hydrophobic and (b) hydrophilic particles. The Gaussian curves are normalized to their maxima for visualization reasons.

Our experimental values can now be directly compared to the theoretical broadening. In absence of chemical inhomogeneities and neglecting the line tension effects, the full width at half maximum (FWHM) of the particle position distribution of monodisperse particles with  $\sim 330$  nm radius is given

by  $FWHM = \sqrt{\ln 2 / \beta} = 3\%$ , where  $\beta = \frac{4\pi R^2 \gamma_{o/w}}{k_B T}$ .<sup>[8]</sup> This translates into a theoretical broadening of the contact angle distributions  $\sigma_{\theta,th} = 2^\circ$ , which equals  $\sigma_{\theta,p}$  for hydrophobic particles after deconvolution of  $\sigma_{\theta,total,i}$  (eq. S5). By contrast, we have a mismatch between the theoretical and experimental values  $\Delta\sigma = \sigma_{\theta,p} - \sigma_{\theta,th} = 3.5^\circ$  for hydrophilic beads. We attribute this discrepancy to the higher affinity of PEG-552 for the hydrophilic silica particles which might change the interaction between the colloids and the interface.

### 3.4 Extended contact angles and line tension data of hydrophobic and hydrophilic particles

In the following we present the full data range of contact angles computed for hydrophobic (Fig. S11a) and hydrophilic (Fig. S11b) particles, respectively, when straddling the water-octanol interface, according to eq. S4, eq. S2.

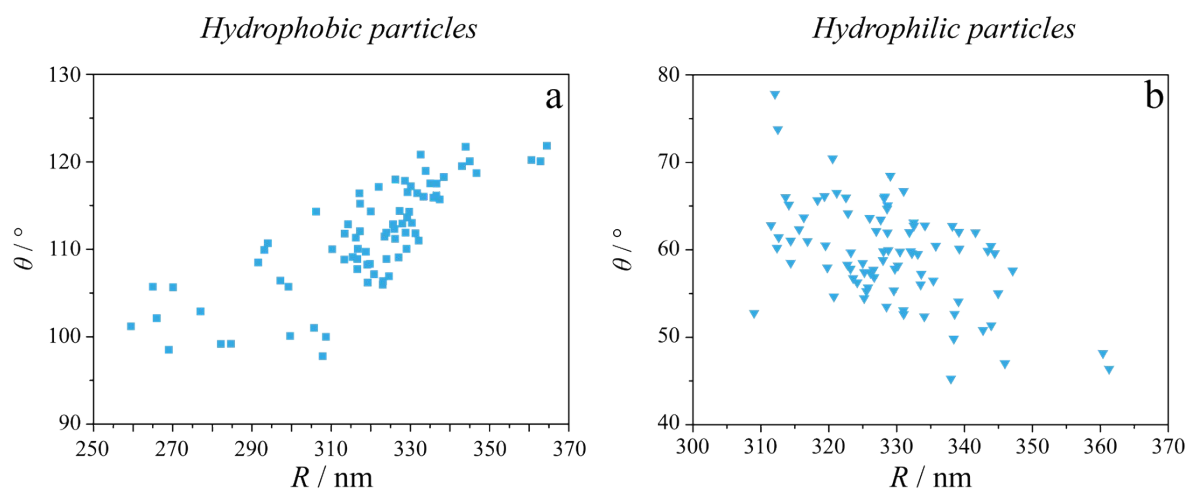


**Fig. S11** Extended data of contact angle  $\theta$  as function of radii,  $R$ , for (a) hydrophobic and (b) hydrophilic particles.

### 3.5 Impact of the iPAINT probe on the single-particle contact angle measurement

As a probe in our iPAINT experiments, we utilize a polymer-conjugated photo-activatable dye. Its adsorption at the interface reduces the interfacial tension,<sup>[9]</sup> which in turn affects the measured single-particle contact angle values. To assess the extent of this effect, we perform a number of experiments, which are described in the following section.

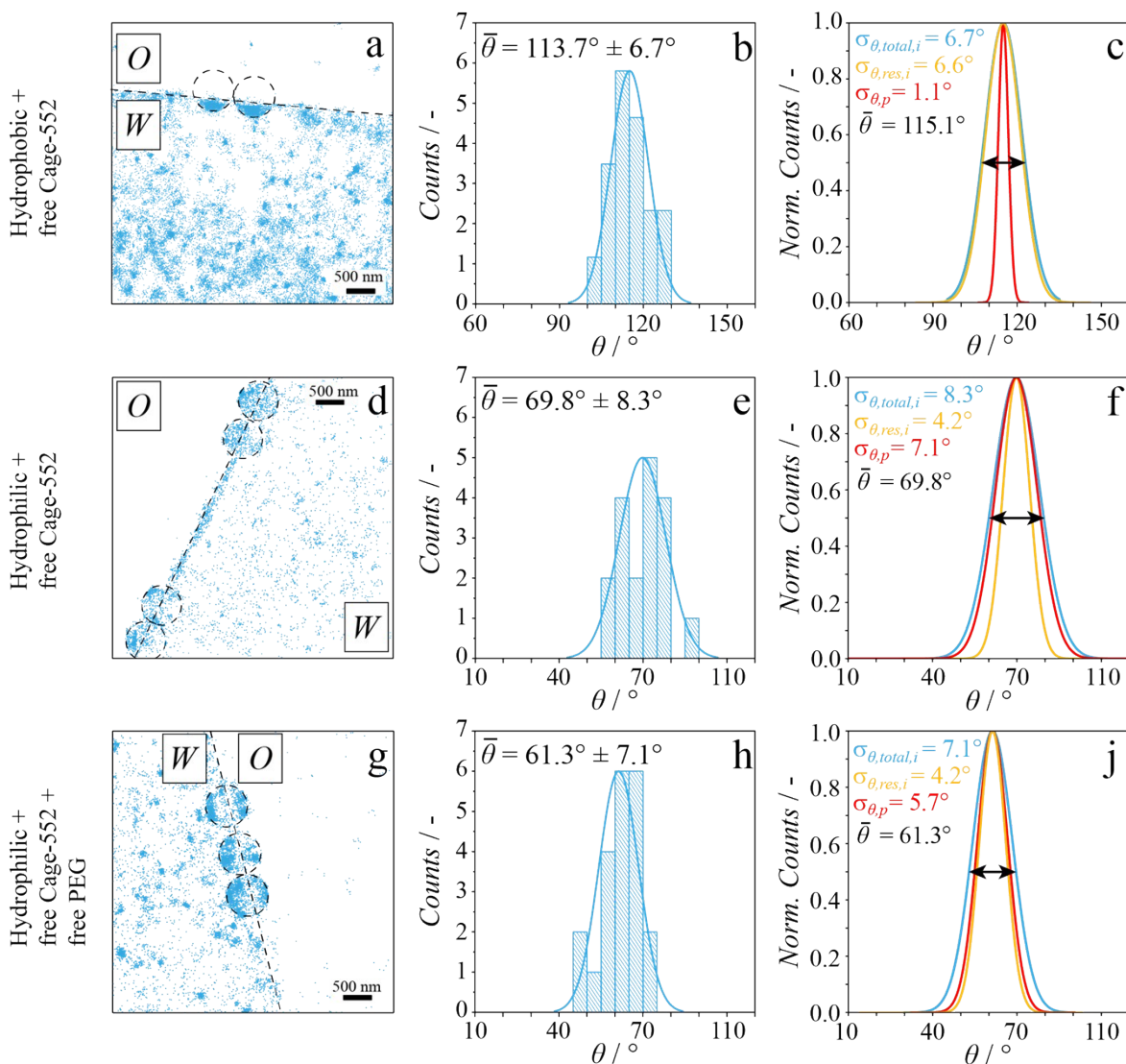


**Fig. S12** Quantification of the effect of iPAINT probes on particles contact angles. iPAINT imaging of hydrophobic (a), hydrophilic (d) particles (black dashed circles) adsorbed at the fluid interface (black dashed line) by using freely diffusing Cage-552 dye. Contact angle distribution of  $\sim 20$  hydrophobic (b), and hydrophilic (e) particles adsorbed at the water-octanol interface, and deconvolution of the imaging resolution ( $\sigma_{\theta,res,i}$ ) and particle variability ( $\sigma_{\theta,p}$ ) in the contact angle distribution on hydrophobic (c), and hydrophilic (f) particles. (g) iPAINT imaging by freely diffusing Cage-552 dye of hydrophilic particles in presence of polyethylene glycol (PEG) at the water-octanol interface. (h) Related contact angle distribution of  $\sim 20$  hydrophilic particles, and (j)

subsequent deconvolution of the imaging resolution ( $\sigma_{\theta,res,i}$ ) and particle variability ( $\sigma_{\theta,p}$ ) in the contact angle distribution.

We start by iPAINT experiments on hydrophobic (Fig. S12a) and hydrophilic (Fig. S12d) particles using as a probe the dye itself, Cage-552, instead of the polymer-conjugated dye, PEG-552. As shown in Fig. 2 of the main text, the particles can be located with high accuracy at a fluid interface. We determine a mean contact angle for the hydrophobic colloids is  $\bar{\theta} = 113.7^\circ \pm 6.7^\circ$ , which is  $2.2^\circ$  higher than the one reported when using the PEG-552 as a probe ( $\bar{\theta} = 111.5^\circ \pm 7.0^\circ$ ). This means that the presence of the polymer slightly affects the system. An even larger difference is observed for the hydrophilic particles:  $\bar{\theta} = 69.8^\circ \pm 8.3^\circ$  (Cage-552) vs.  $\bar{\theta} = 59.5^\circ \pm 6.9^\circ$  (PEG-552). To test whether this effect originates from the presence of the PEG chains, we image the hydrophilic particles by iPAINT using free Cage-552 and free PEG chains in solution (Fig. S12g). If the presence of PEG is the key factor, we should retrieve the same contact angle calculated in Fig. 2 of the main text. From iPAINT experiments on hydrophilic particles in the presence of Cage-552 and free PEG in solution we obtain  $\bar{\theta} = 61.3^\circ \pm 7.1^\circ$  (Fig. S12h). This value is  $\sim 9^\circ$  lower than the values obtained for Cage-552 (Fig. S12e,  $\bar{\theta} = 69.8^\circ \pm 8.3^\circ$ ) and comparable to that obtained using PEG-552 (Fig. 2 in the main text), suggesting that the difference is due to the interfacial adsorption of PEG.

Since the presence of PEG influences the measured contact angles, theoretically it would be better to image with Cage-552 rather than PEG-552. However, the identification of the two phases is not as neat as when PEG-552 is utilized. In fact, the presence of the polymer as carrier of the photo-activatable moieties confines the probes to diffuse solely in the aqueous phase ( $\sim 85$  localizations per  $\mu\text{m}^2$  in the water phase vs.  $\sim 15$  localizations per  $\mu\text{m}^2$  in the oil phase, Fig. 2 in the main text), allowing for a clear identification of the two phases. Regarding the fluid interface, the design of the probe is such that the hydrophobic part stays in the oil phase and the hydrophilic part in the water phase, due to its amphoteric character. In absence of the PEG chain, the hydrophobicity of the Cage-552 dye alone reduces its partitioning between the two phases, resulting in similar single-molecule localization densities ( $\sim 75$  and  $\sim 53$  localizations per  $\mu\text{m}^2$  for water vs. oil, respectively). This necessitates the application of more stringent density filters to ensure precise visualization of both the interface and the particle positions. Unfortunately, this leads in turn to fewer localizations per particle, impeding their full reconstruction.

### 3.5.1 Interfacial tension and macroscopic contact angle measurements.

We performed interfacial tension measurements by pendant droplet tensiometer to quantify the macroscopic effect of the iPAINT probes on the system at the optimum concentration for the imaging procedure ( $0.5 \mu\text{M}$ ). Water-octanol interfacial tension resulted in  $7.78 \pm 0.05 \text{ mN/m}$ . When the water phase is enriched with PEG-552 ( $0.5 \mu\text{M}$ ), the interfacial tension obtained is  $7.96 \pm 0.08 \text{ mN/m}$ . Similarly, the interfacial tension of water-octanol in presence of only Cage-552 dye ( $0.5 \mu\text{M}$ ) measured is  $7.88 \pm 0.03 \text{ mN/m}$ . In fig. S13 we present the pendent droplets in water, PEG-552 and Cage-552, respectively (scale bar = 1 mm):

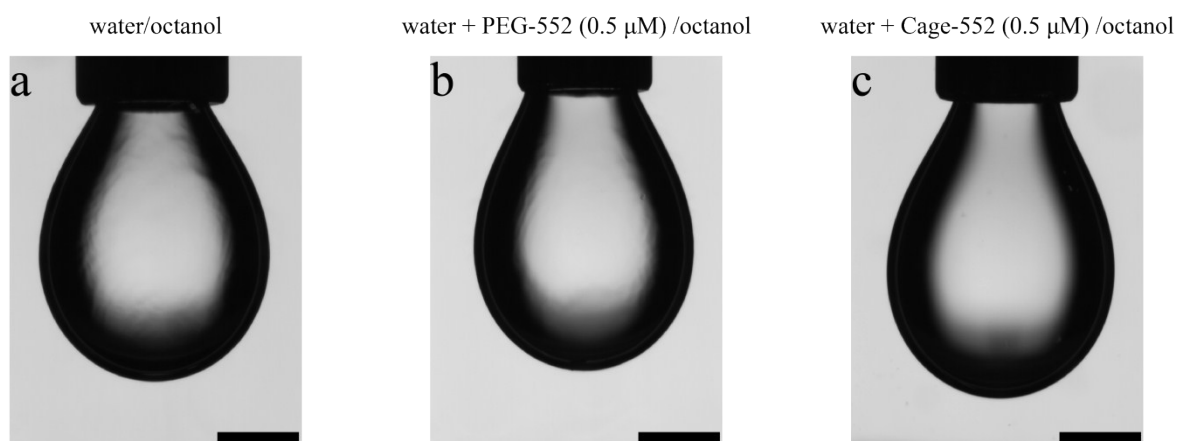


**Fig. S13** Interfacial tension measurements of (a) water-octanol, (b) PEG-552 solution (0.5  $\mu\text{M}$ )-octanol, and (c) Cage-552 solution (0.5  $\mu\text{M}$ )-octanol. Scale bar 1 mm.

We also performed macroscopic contact angle measurements of water droplets, in presence of the iPAINT probes, on a silica substrate surrounded by octanol to macroscopically mimic the experimental conditions set for iPAINT measurements. We retrieved a mean contact angle of  $\theta = 67.8^\circ \pm 2.5^\circ$  for the hydrophilic silica substrate (Fig. S14).

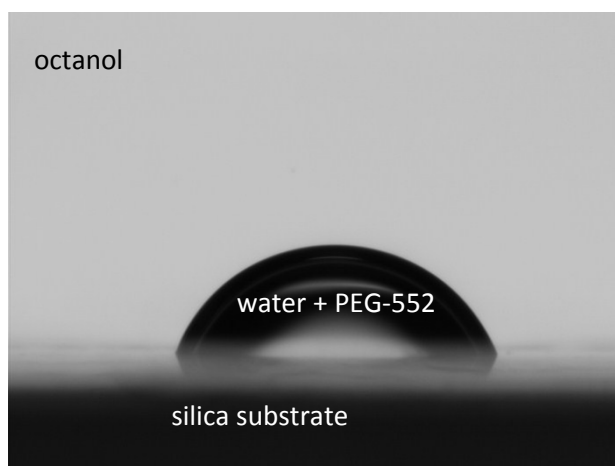


**Fig. S14** Macroscopic contact angle measurement of a water droplet enriched in PEG-552 probes (0.5  $\mu\text{M}$ ) on a hydrophilic silica substrate, surrounded by the octanol phase.

## 4. Ellipsoidal particles

### 4.1 Synthesis and TEM characterization of polystyrene ellipsoidal particles

Briefly, monodisperse sulfate latex spheres of 1  $\mu\text{m}$  in diameter (Invitrogen) are embedded into a poly(vinyl alcohol) (PVA) matrix and subsequently put in a silicon bath at a temperature above the glass transition temperature but below the melting temperature of the material. The film undergoes an uniaxial stretching as reported in literature.<sup>[10]</sup> All spheres are exposed to a controlled plastic deformation to prolate ellipsoids with a given aspect ratio.<sup>[11]</sup> The ellipsoids here used present an aspect ratio of  $4.9 \pm 0.5$  (Fig. S15c). Data reported by Coertjens *et al.* demonstrates a constant volume deformation of the particles under stretch, and that they keep an ideal prolate shape.<sup>[11]</sup> Afterwards, the film strips are kept under stretching and cooled down by air flow. Several washing steps involving isopropanol-water mixture and MilliQ-water, followed by an heating step at 50  $^{\circ}\text{C}$  and subsequent ultrasonication are needed to clean the ellipsoids, after the PVA film is dissolved.<sup>[10,11]</sup> TEM images of the prolate ellipsoids with aspect ratio of  $4.9 \pm 0.5$  are conducted on a FEI Tecnai 20, type Sphera TEM instrument operating at 200 kV (LaB6 filament) with a bottom mounted 1024  $\times$  1024 Gatan msc 794TM CCD camera. Samples are prepared using carbon-coated 200 mesh copper grids.

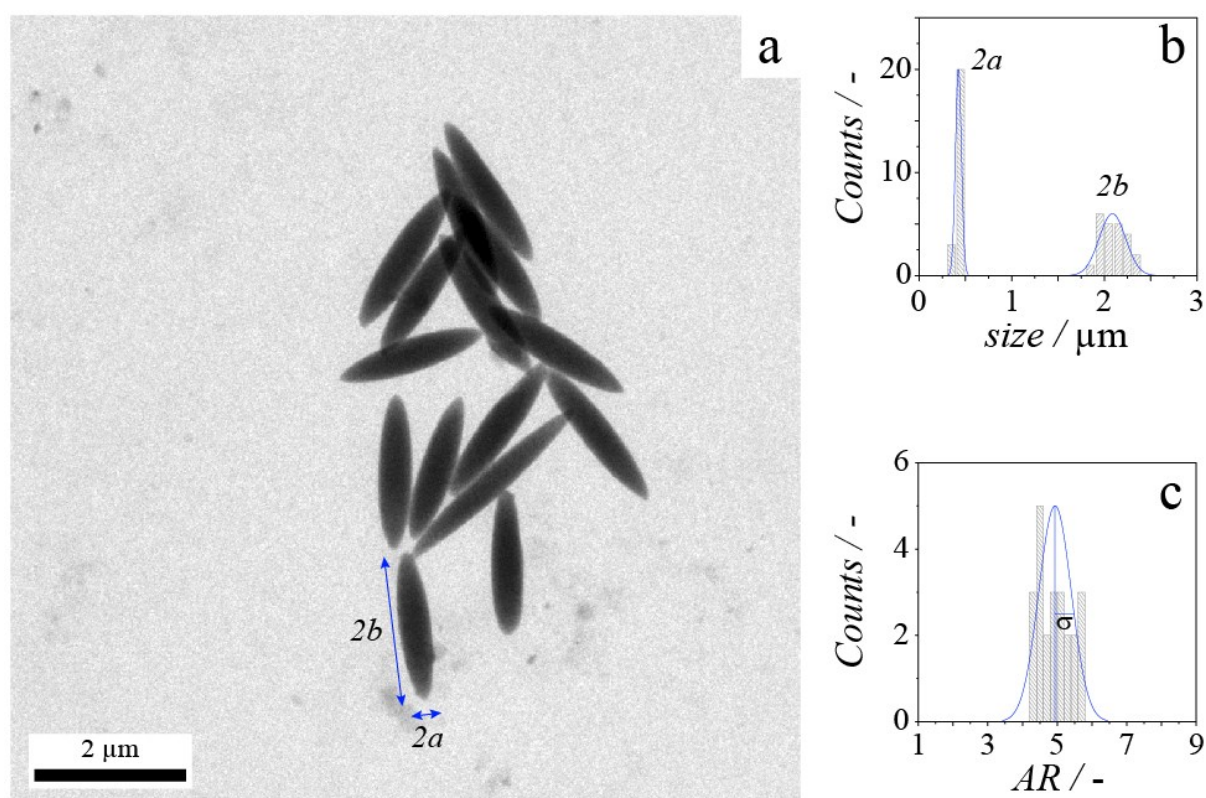


**Fig. S15** Characterization of polystyrene ellipsoids. (a) TEM picture of ellipsoidal particle with major axis  $2b = 2087 \pm 142$  nm, and minor axis  $2a = 425 \pm 32$  nm. The aspect ratio  $AR = b/a = 4.9 \pm 0.5$ . (b-c) Distributions of major and minor axis and aspect ratio of the ellipsoidal particles.

## 4.2 Calculation of contact and polar angles of individual ellipsoidal particles

Here we present how to calculate the contact angle ( $\theta$ ) for ellipsoidal particles oriented parallel to the interface (Fig. S16a), and the polar angle ( $\varphi$ ) for those in the 'arrested' configuration oblique to the interface (Fig. S16b) from iPAINT measurements.

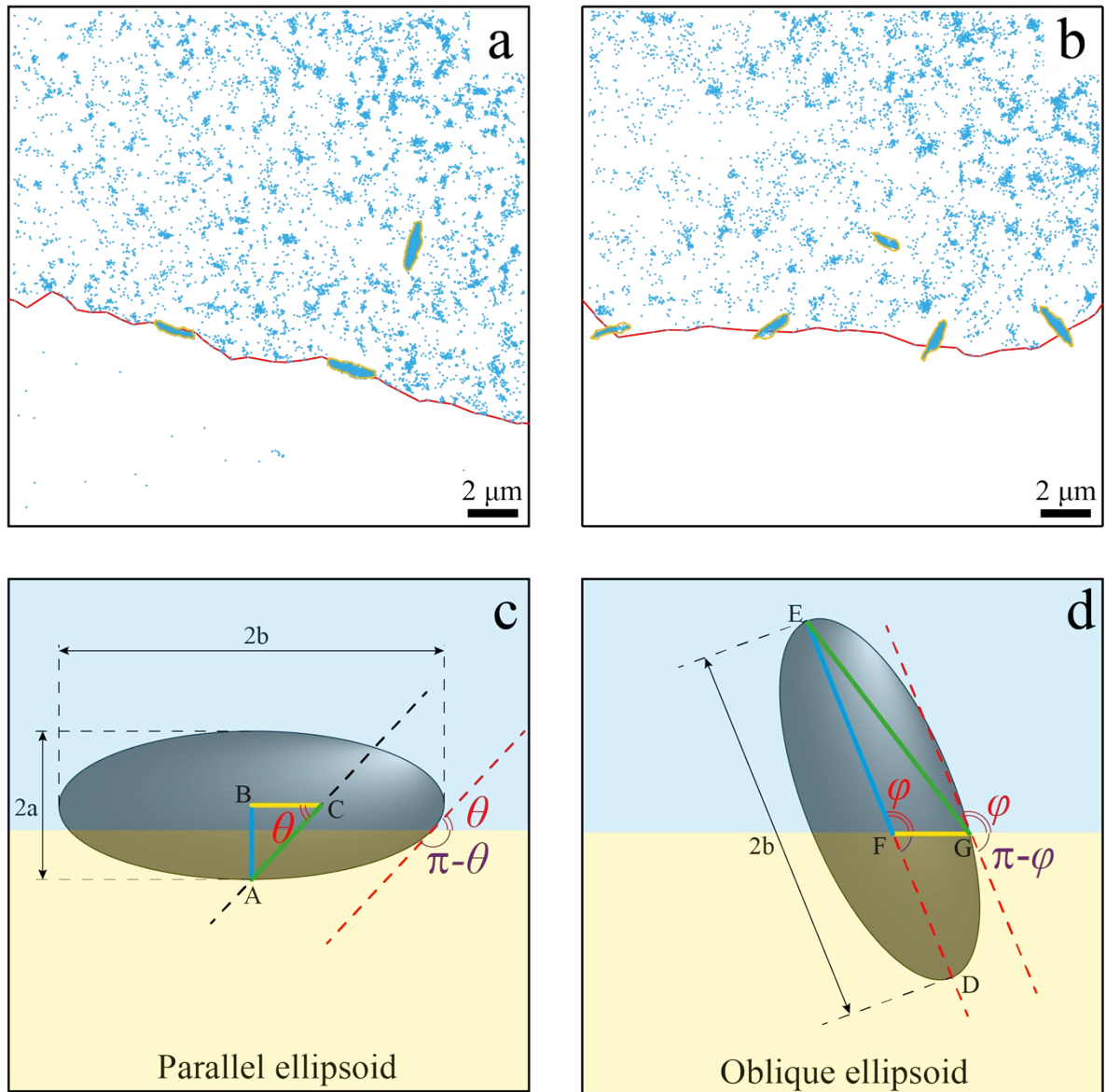


**Fig. S16** Top row: ellipsoids at fluid interfaces imaged by iPAINT. (a) Polystyrene ellipsoidal particles laying parallel and (b) obliquely at the water-decane interface. Both iPAINT probes and ellipsoids are dispersed in the aqueous phase, therefore the entire colloids are homogeneously labelled (blue dots). The orange line along the ellipsoids perimeter and the red line to define the interface are obtained by  $\alpha$ -shaping.<sup>[12]</sup> Bottom row: representative cartoon of an ellipsoidal particle at a fluid interface. The schematics illustrate the relevant dimensions  $\overline{AB}$ ,  $\overline{BC}$  and  $\overline{AC}$  to measure  $\theta$  (eq. S8), and  $\overline{EF}$ ,  $\overline{FG}$ , and  $\overline{EG}$  to calculate  $\varphi$  (eq. S9).

To calculate the contact angle  $\theta$  of an ellipsoid oriented flat at the interface we proceed to the determination of segments  $\bar{AB}$ ,  $\bar{BC}$  and  $\bar{AC}$  (Fig. S16c). We start with drawing the tangent to the particle at the three-phase contact line (red dashed line in Fig. S16c), which defines the contact angle  $\theta$ . Then we translate the tangent until it intersects the contour of the particle at its minor axis  $2a$  (black dashed line in Fig. S16c). The half of the minor axis will be defined as the segment  $\bar{AB}$  (blue line in Fig. S16c). We then highlight the major axis of the particle and, from its intersection with the tangent, we define the point  $C$  (yellow line in Fig. S16c). Then, we connect point  $C$  and point  $A$  to define the segment  $\bar{AC}$  (green line in Fig. S16c). The angle in  $C$  is the contact angle  $\theta$ , and it can be computed as:

$$\cos \theta = \frac{\bar{AC}^2 + \bar{BC}^2 - \bar{AB}^2}{2\bar{AC} \cdot \bar{BC}} \quad (S8)$$

Aiming to obtain  $\varphi$  for the particles with an oblique orientation, we measure the length of the segments  $\bar{EF}$ ,  $\bar{FG}$ , and  $\bar{EG}$  in the iPAINT image, as depicted in figure S13d. For the oblique or tilted configuration, the polar angle is given by the orientation of the major axis with respect to the fluid interface. Hence, we draw the major axis ( $2b$ ) of the particle as the segment  $\bar{DE}$  in Fig. S16d. We define the segment  $\bar{EF}$  along the segment  $\bar{DE}$  as the segment that goes from the tip of the ellipsoid in the water phase to the position of the interface (blue line in Fig. S16d). We determine the segment  $\bar{FG}$  (yellow line in Fig. S16d) following the interface from the point  $F$  till the contour of the particle (point  $G$ ). Then we join point  $G$  and point  $E$  in the segment  $\bar{EG}$  (green line in Fig. S16d). The angle in  $F$  is the polar angle  $\varphi$ , and it can be calculated from:

$$\cos \varphi = \frac{\bar{EF}^2 + \bar{FG}^2 - \bar{EG}^2}{2\bar{EF} \cdot \bar{FG}} \quad (S9)$$

### 4.3 Quantifying the orientation of ellipsoids at the liquid-liquid interface

We set out to unambiguously define the orientation of the ellipsoids at the fluid interface using the polar angle,  $\varphi$ . This corresponds to the angle between the interface and the major axis of the particle. We consider particles with  $-5^\circ < \varphi < 5^\circ$  to be oriented parallel to the interface (Fig. S17c), while  $85^\circ < \varphi < 95^\circ$  are taken as normal to the interface (Fig. S17b). All the  $\varphi$  values not included in the intervals mentioned before are considered oblique (Fig. S17a). Note that we use a minimal interval of  $10^\circ$  in view of the experimental resolution of  $\sim 3^\circ$  due to the  $\sim 20$  nm lateral resolution in iPAINT. Applying the above described classification on iPAINT images of ellipsoidal particles at decane-water interface, it reveals that most ellipsoids ( $>30$  examples) lay parallel, as expected. In our experiments, we find roughly 9% normally aligned particles ( $<5$  cases) and roughly  $\sim 36\%$  of the particles in an oblique orientation (20 particles). The distribution of polar angles for each orientation is shown in Fig. S17d.

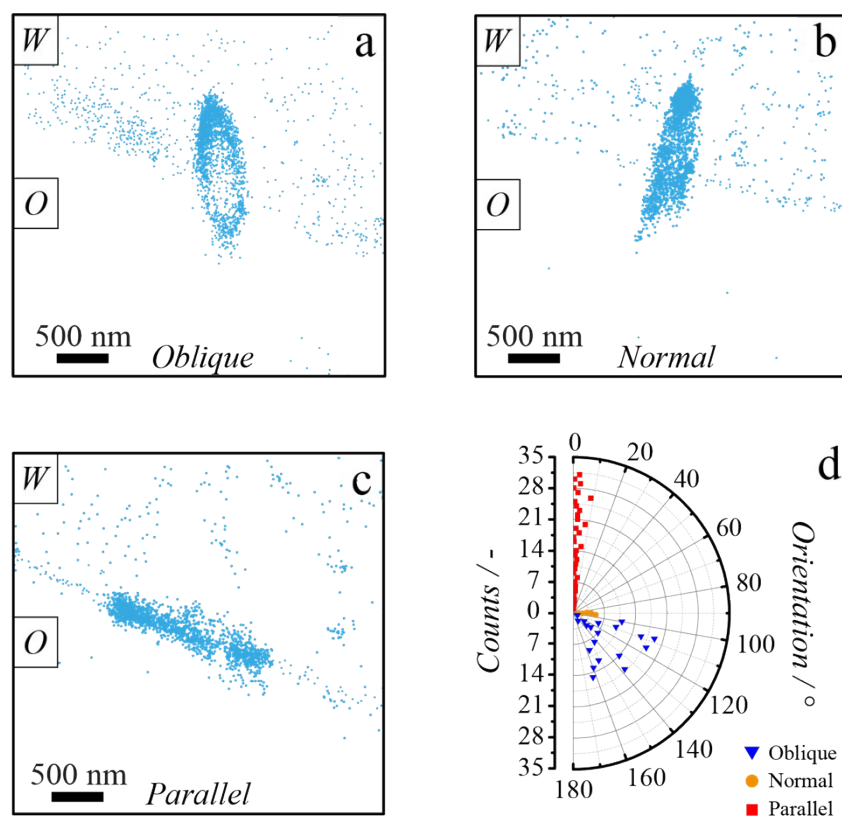


**Fig. S17** Orientation of ellipsoidal particles at the fluid interface. (a-c) Exemplary iPAINT images of ellipsoids oriented oblique, normal and parallel to the water-decane interface. The long axis of the ellipsoids gives the orientation respect to the interface; within a range of  $\pm 5^\circ$  (larger than the resolution of the iPAINT method) we discriminate among different orientations. (d) Quantification of the parallel (red closed squares), normal (orange closed circles) and oblique (blue closed triangles) ellipsoids as a function of their orientation  $\varphi$ . The absolute value of  $\varphi$  is displayed for the parallel ellipsoids.

#### 4.4 Single ellipsoidal particle contact-angle measurement

The results of the iPAINT experiments on particles lying flat at the interface, in the equilibrium position (Fig. S18a), is depicted in Fig. S18b. We obtain a mean contact angle  $\bar{\theta} = 42.7^\circ \pm 6.1^\circ$  (Fig. S18b) for ellipsoids parallel to the fluid interface with the same surface chemistry and aspect ratio, which is somewhat lower than the values from FreSca ( $\bar{\theta} = 66^\circ \pm 12^\circ$ ).<sup>[11]</sup>

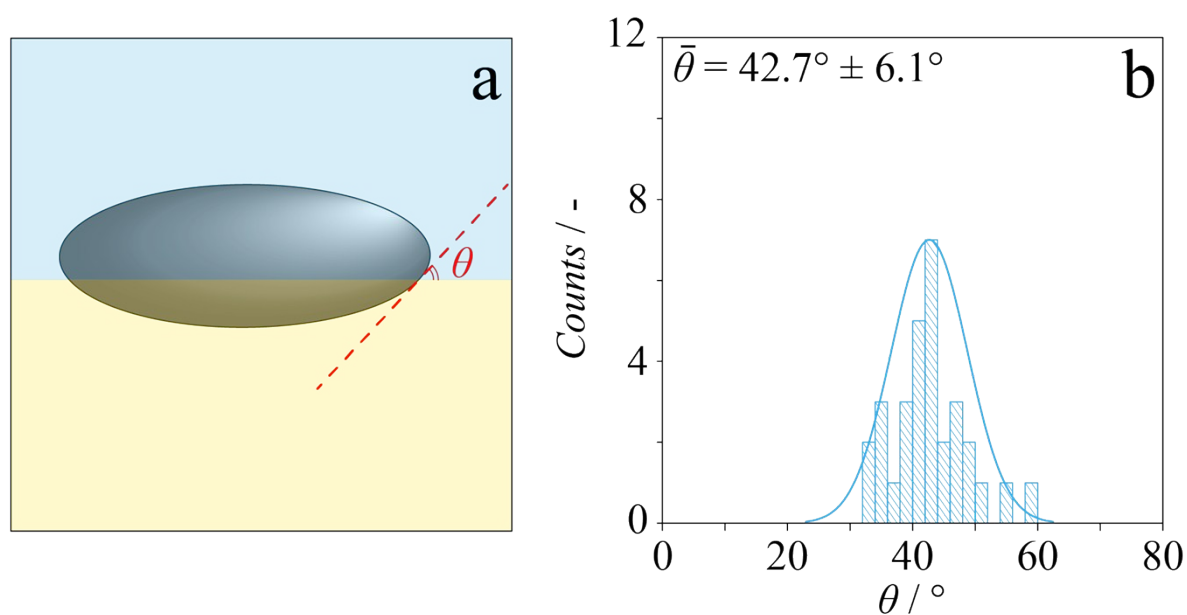


**Fig. S18** Contact angle  $\theta$  measurements of individual ellipsoids lying flat at a fluid interface. (a) Schematic representation of an ellipsoid adsorbed parallel to an oil-water interface. The schematic highlights the three-phase contact angle  $\theta$ . For  $\theta < 90^\circ$  the centre of mass of the particle resides in the water phase. (b) Distribution of contact angles of the ellipsoids.

#### 4.5 Pivoting of ellipsoids at the fluid interface

iPAINT imaging surprisingly show ellipsoids in an oblique orientation at fluid interfaces (Fig. 5e in the main text, Fig. S16, Fig. S17). We believe these particles are captured in a non-equilibrium state, defined as ‘arrested configuration’. This specific orientation captured in several iPAINT images is due to the ellipsoidal particle settling on the coverslip while pivoting within the interface to reach their equilibrium position (Fig. S19a). To test this idea, we plot  $\varphi$  vs. the distance to the interface of the center of mass  $z_{CM}$ . These quantities are related to the translational ( $z_{CM}$ ) and rotational ( $\varphi$ ) motion of the particles. Interestingly, we find a linear relation between  $\varphi$  and  $z_{CM}$  (Fig. S19b), as predicted for particles that pivot at the interface due to pinning of the three-phase contact line, which exerts a tangential force on the particle. Wang *et al.* recently observed such pivoting of ellipsoids at a fluid interface by holographic microscopy combined with optical tweezers.<sup>[13]</sup> The authors attributed the linear dependence of  $\varphi$  on  $z_{CM}$  to the pinning of the interface on defects on the surface of rough sulfate-functionalized polystyrene particles of  $\sim 2 \mu\text{m}$  in length.<sup>[6,14,15]</sup>

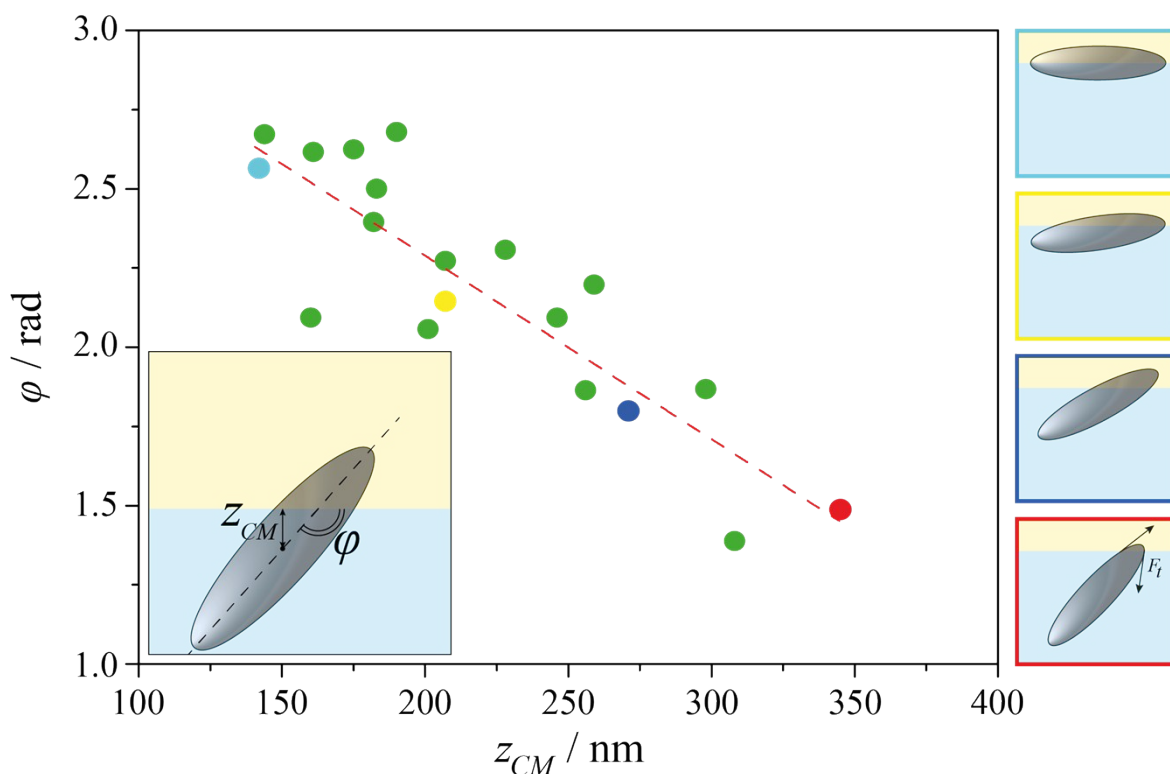


**Fig. S19** Polar angle  $\varphi$  of oblique ellipsoids vs. the height of the center of mass,  $z_{CM}$ . The height of the center of mass of ellipsoids oriented oblique to the fluid interface evolves linearly with the polar angles, implying translation and rotation of the particle at the fluid interface. The panels on the right side show schematics of an ellipsoidal particle breaching the fluid interface showing a monotonic decrease in height of the center of mass and polar angle. The panels are color-coded with the data points in the graph. Green data points are intermediate states between the coloured ones.

## 5. References

- 1 H. Deschout, F. Cella Zancchi, M. Młodzianoski, A. Diaspro, J. Bewersdorf, S.T. Hess, K. Braeckmans, *Nat. Methods*, 2014, **11**, 253-266.
- 2 N. Vilanova, I. de Feijter, I.K. Voets, *J. Vis. Exp.*, 2016, **110**, e53934-1-7.
- 3 A.K. van Helden, J.W. Jansen, A. Vrij, *J. Colloid Interf. Sci.*, 1981, **81**, 354-368.
- 4 M. Zanini, L. Isa, *J. Phys.: Condens. Matter*, 2016, **28**, 313002-1-25.
- 5 L. Isa, F. Lucas, R. Wepf, E. Reimhult, *Nat. Commun.*, 2011, **2**, 438-1-9.
- 6 D.M. Kaz, R. McGorty, M. Mani, M.P. Brenner, V.N. Manoharan, *Nat. Mater.*, 2012, **11**, 138-142.
- 7 R.V. Hogg, J.W. McKean, A.T. Craig, *Introduction to Mathematical Statistics*, 2006, 6th ed., Pearson, UK.
- 8 F. Bresme, M. Ottel, *J. Phys.: Condens. Matter*, 2007, **17**, 413101-1-33.
- 9 M.A. Cohen Stuart, W.M. de Vos, F.A.M. Leermakers, *Langmuir*, 2006, **22**, 1722-1728.
- 10 K.M. Keville, E.I. Franses, J.M. Caruthers, *J. Colloid Interface Sci.*, 1991, **144**, 103-126.
- 11 S. Coertjens, P. Moldenaers, J. Vermant, L. Isa, *Langmuir*, 2014, **30**, 4289-4300.
- 12 S. Lou, X. Jiang, P.J. Scott, *Proc. R. Soc. A*, 2013, **469**, 20130150.
- 13 A. Wang, W.B. Rogers, V.N. Manoharan, *Phys. Rev. Lett.*, 2017, **119**, 108004-1-5.
- 14 V.N. Manoharan, *Nat. Mater.*, 2015, **14**, 869-870.
- 15 G. Boniello, C. Blanc, D. Fedorenko, M. Medfai, N.B. Mbarek, M. In, M. Gross, A. Stocco, M. Nobili, *Nat. Mater.*, 2015, **14**, 908-911.